Bone Mineral Density modelled as a Random Field: a Feasibility Study on Pelvic Bone

Petr Henyš[a], Miroslav Vořechovský[b], Michal Kuchař[c], Axel Heinemann[e], Jiří Kopal[a], Benjamin Ondruschka[e], Niels Hammer[d]

[a]*Institute of New Technologies and Applied Informatics, Faculty of Mechatronics, Informatics and Interdisciplinary Studies, Technical University of Liberec, Studentská 1402/2, 461 17 Liberec, Czech Republic*
[b]*Department of Structural Mechanics, Faculty of Civil Engineering, Brno University of Technology, Veveří 331/95, 602 00 Brno, Czech Republic*
[c]*Department of Anatomy, Faculty of Medicine in Hradec Králové, Charles University, Šimkova 870, 500 03, Hradec Králové, Czech Republic*
[d]*Department of Macroscopic and Clinical Anatomy, Medical University of Graz, Auenbruggerpl. 2, 8036 Graz, Austria*
[e]*Institut für Rechtsmedizin, Universitätsklinikum Hamburg-Eppendorf, Butenfeld 34, 22529 Hamburg, Germany*

Abstract

Population variability and correlations in bone mineral density can be described by a spatial random field, which can be inferred from the routine computed tomography (CT) data. Random fields were simulated by transforming pairwise uncorrelated Gaussian random variables into correlated variables through the spectral decomposition of age-detrended correlation matrix estimated from CT. The validity of random field model was demonstrated on spatio-temporal analysis of *bone mineral density* and *bone mineral content*. The similarity of CT samples and that generated from random fields was analyzed with *energy distance* metric. It was found that the bone mineral density random field was approximately Gaussian/slightly left-skewed/strongly right-skewed in various locations. However, bone mineral content could be well simulated with the proposed Gaussian random field and that of energy distance, i.e., a measure to quantify discrepancies between two distribution functions, is convergent with respect to the number of correlation eigenpairs. The proposed random field allows for enriching computational biomechanical models with variability in bone mineral density, which could increase the model usability and provide a step forward in digital twin paradigm.

Keywords: shape registration, Karhunen-Loève expansion, finite element method, uncertainties, bone mineral content

Introduction

Bone structural and intrinsic properties are inhomogeneous, and vary across the multiple spatial and temporal scales and population. It was documented that bone properties vary at collagen fibrils level as well as lamellae level and naturally vary across the anatomical sites [1, 2]. Structural inhomogeneities are related to bone fragility and toughness [3, 4, 5, 6]. The *bone mineral density* (BMD) is widely used study the bone properties. BMD is remarkably inhomogeneous [3, 7], connected to bone elasticity and fracture risk [8, 9, 10].

The spatial variation of BMD was previously analyzed through variograms [11, 12], where the authors attempted to enhance the fracture risk prediction ability related to BMD. Other studies demonstrated significant correlations of parameters of BMD variogram with trabecular bone morphological measures and bone strength [13, 14]. On the opposite, the relation of vertebrae strength and variogram parameters were not significantly correlated in [15]. Dong et al. [16] demonstrated that bone elasticity variation at nano scale can be described as a random field. Due to bone complex behavior controlled by many factors including remodeling process, stationarity and isotropicity assumptions will likely be violated, but to the authors' knowledge, this has never been investigated. Recent studies emerged the describing bone properties as a random field. Desceliers et al. [17] introduced a simplified random field model of cortical bone, but not yet calibrated on clinical data. Another study showed that trabecular structure can be generated by an inverse Monte Carlo simulation on Voronoï cells which exhibited a good match with trabecular morphology [18]. In the study of Luque et al. [19], a density random field of trabecular *region of interest* (ROI) was modelled with directionally separable autocorrelation functions based on CT. But this study lacks sufficient samples and moreover a stationary correlation kernel was estimated only on a ROI of a small size.

Study Aim & Outline

This given study aimed to analyze the spatio-temporal variability of BMD and to demonstrate BMD as a random field. Firstly, a shape registration algorithm was used to geometrically align CTs (Section Shape Registration). In a next step, the Karhunen-Loève expansion (KLE) was employed to simulate BMD as random field with Gaussian coefficients, see Section Karhunen-Loève Expansion. The new realizations of BMD based on model of random field were validated on bone mineral content (BMC), which can be considered as a global measure of bone quality. Further, the so-called *energy distance* [20] was computed between random field of BMD known from CTs and that generated with KLE, which

*Corresponding author
Email address: michal.kuchar@lfhk.cz (Michal Kuchař)

is evaluated locally to see how similar are the distributions point-wise and globally as an integral measure (Section Validation Measures); see the flow chart in Figure 1.

Materials and Methods

CT Data Collection

The anonymized retrospective CT data of 97 females and 88 males were randomly taken from routine examinations in the Faculty Hospital in Hradec Králové under ethical approval 202102IO2P. The CT resolution of the dataset was $0.8 \times 0.8 \times 0.8$ mm (Siemens Definition AS+, Siemens Definition 128, both Siemens AG, Erlangen, Germany; 120–130 kV using CareDose, reconstruction kernel 80–90, bone algorithm). The inclusion criteria were as follows: abdominal CT scans, bones without any trauma, and an age range of 20 years or older. The sample population age per sex is in range 22–88 years, divided into 10 bins, where each bin contains more than 5 samples. The pelvic bone geometry implicitly defined by Hounsfield (HU) field was extracted with interactive segmentation software MITK-GEM [21]. The CT scans were calibrated internally resulting in BMD [22]. Only the right hand side pelvic bone was considered because no significant difference was explored between the left and right sides.

Shape Registration

The estimation of the random field density requires a universal description of bone locations among all experimentally studied bones using a single reference/template bone shape. This is achieved by introducing a fixed metric for spatial or temporal locations per sample to evaluate at. This requirement is violated for bone samples because each sample has different size and different shape. However, bone samples are anatomically and topologically equivalent. This implies the existence of a point correspondence between two shapes under some suitable class of bijective maps and similarity metrics. To find such correspondence, a non-linear mapping was found with help of diffeomorphic based registration algorithm ANTs, see [23]. But before non-linear mapping being used, the rigid and affine transforms are realized for initial global alignment of bones in datasets. The similarity of bone shapes was measured with a modified intensity-based criterion called the demons-like metric. This metric provides best accuracy/speed balance among the other metrics tested (mean-squared difference, cross-correlation, mutual information) [23, 24]. In order to minimize a registration error, a template bone shape, which is an estimation of a sample mean shape, was estimated according to [25, 23].

Finite Element Projection of BMD Field

The template geometry described by implicit HU field was transformed to a triangulated surface by marching cube algorithm [26]. The resultant triangular mesh was used to build the volume tetrahedral mesh (fTetWild [27]).

There are two sets of finite element (FE) models. The first set consists of validation models. The morphed BMD fields from dataset were projected onto a discontinuous FE space constructed on template mesh. All samples in the dataset shared the same geometry domain and finite element space. The correlation matrix of BMD can then be estimated. The FE models in the second set contain BMD fields simulated by KLE on the template geometry. The FE mesh size was estimated based on the auxiliary convergence study where the BMC difference between two mesh refinements below 5% was considered as converged. The resultant number of degrees of freedom (DOFs) was roughly $M \approx 0.7 \cdot 10^6$.

Karhunen-Loève Expansion

The data set was split into two sets according to sex in order to capture sex differences. Consequently, the relation between age and BMD was analyzed and linear regression was used to separate deterministic trend composing of intercept (sample mean) $\boldsymbol{\rho}_0$ and slope $\boldsymbol{\rho}_1$ from matrix $\mathbf{X}$.

A random field $\boldsymbol{\rho}(\mathbf{x}) \in \Omega$ is not known explicitly, but only through a set of N standardized realizations projected onto the template bone:

$$\mathbf{X} = \{\mathbf{X}_1, \mathbf{X}_2, \ldots, \mathbf{X}_M\},\ \mathbf{X} \in \mathbb{R}^{M,N} \tag{1}$$

The projected realizations are evaluated at DOF coordinates, from which the matrix of realizations $\mathbf{X}$ is build. The empirical correlation matrix $\mathbf{C}$ is estimated as $\frac{1}{N-1}\mathbf{X}\mathbf{X}^T$. The discretized random field can be viewed as a set of correlated random variables. Sample paths of Gaussian random fields can then be generated by transforming uncorrelated Gaussian random variables into correlated space [28, 29]. One possible linear mapping between the uncorrelated and correlated Gaussian random vectors is via KL expansion. This expansion involves eigen-decomposition of the correlation matrix (or the covariance function having the role of covariance kernel in the continuous version of KL expansion). In order to compute the KL decomposition of $\mathbf{C}$, the associated discrete eigenvalue problem must be solved [30]:

$$\mathbf{C}\boldsymbol{\Psi} = \mathbf{D}\boldsymbol{\Psi} \tag{2}$$

where $\boldsymbol{\Psi} \in \mathbb{R}^{M,M}$ is a matrix of eigenvectors and $\mathbf{D} = \mathrm{diag}(\lambda_1, \lambda_2, \ldots, \lambda_M)$ is the diagonal matrix of eigenvalues. The full population of correlation matrix $\mathbf{C}$ is impossible as it is dense, moreover the rank of the matrix $\mathbf{C}$ is N only and hence we adopt an alternative solution of the above eigenproblem represented by a suitable matrix decomposition. Considering an economic QR decomposition of $\mathbf{X}$, the matrix $\mathbf{C}$ can be expressed:

$$\mathbf{C} = \mathbf{Q}\mathbf{R}\mathbf{R}^T\mathbf{Q}^T,\ \mathbf{R}\mathbf{R}^T \in \mathbb{R}^{N,N}. \tag{3}$$

Consequently, the singular value decomposition of product $\mathbf{R}\mathbf{R}^T$ is computed:

$$\mathbf{R}\mathbf{R}^T = \mathbf{V}\mathbf{D}\mathbf{V}^T \tag{4}$$

Substitution of Eq. (4) into Eq. (3) leads to:

$$\mathbf{C} = \underbrace{\mathbf{Q}\mathbf{V}}_{\boldsymbol{\Psi} \in \mathbb{R}^{M,N}}\mathbf{D}\mathbf{V}^T\mathbf{Q}^T,\ \mathbf{D} \in \mathbb{R}^{N,N} \tag{5}$$

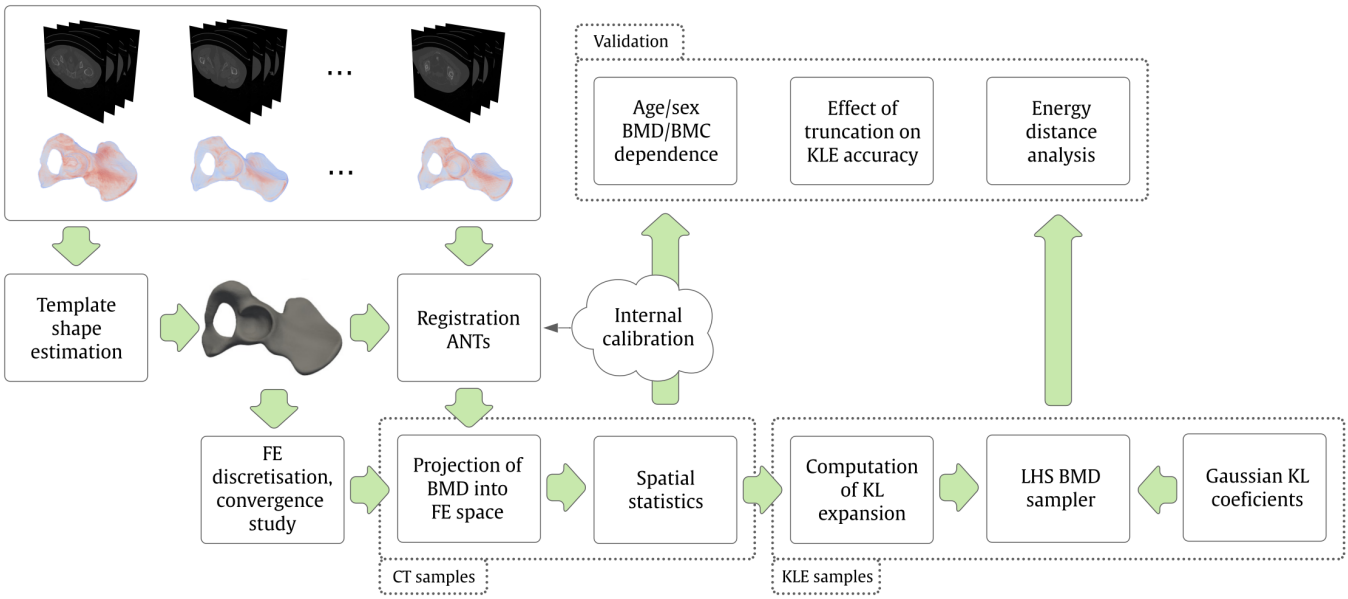

Figure 1: A flowchart of the study.

where $\mathbf{\Psi}$ and $\mathbf{D}$ are the eigenvector and eigenvalue matrices of $\mathbf{C}$. Having the N eigenpairs computed and sorted in decreasing order $\lambda_1 > \lambda_2, \ldots, \lambda_{N-1} > \lambda_N$, the spectral representation of random field $\boldsymbol{\rho}(\mathbf{x})$ can be replaced with truncated discrete KL expansion [30]:

$$\boldsymbol{\rho}(\mathbf{x}) = \boldsymbol{\rho}_0(\mathbf{x}) + \boldsymbol{\rho}_1(\mathbf{x})t + \boldsymbol{\sigma}(\mathbf{x}) \sum_{i=1}^{P} \sqrt{\lambda_i}\theta_i \boldsymbol{\psi}_i(\mathbf{x}) \qquad (6)$$

where the θ_i is zero mean, unit variance ith Gaussian pairwise uncorrelated variable described by $\mathcal{N}(0,1)$, t is a time (age) in range 22–89 years (from CT data sets) and $\boldsymbol{\sigma}(\mathbf{x})$ sample standard deviation.

The truncation in the KLE expressed in Eq. (6) may lead to dramatic computation time savings, since P can be considerably less than the order of correlation matrix (= the number of discretization points), M, and also less than the order N. An appropriate selection of truncation order P can be based on various points of view. The standard way is to control the truncation error in KLE on the decay of the covariance operator's eigenvalues. The eigenvalues play the role of variances of the underlying uncorrelated random variables θ_i which serve as random coefficients of deterministic eigenfunctions/vectors $\boldsymbol{\psi}_i(\mathbf{x})$. Given this interpretation, one can easily control the total amount of variance represented via truncated KLE. Since the correlation matrix $\mathbf{C}$ is positive (semi)definite by definition, the eigenvalues are nonnegative and their sum is known. The eigenvalues can be sorted from the maximum eigenvalue to the minimum one, along with the corresponding eigenvectors (or eigenfunctions). The gradual sum of the sorted eigenvalues serves as an indicator of how much variance is captured by the corresponding subset of eigenmodes. In other words, the expansion can be truncated after taking a subset of P dominant eigenvalues (=variables with the largest variance). The number of modes needed to cover a sufficient variability depends on the reach of autocorrelation function: when the autocorrelation length is high compared to the domain dimensions, usually only a small subset of eigenpairs is necessary for a given truncation error. Furthermore, it can be shown that KL expansion is optimal with respect to the global mean-squared error among all series expansions of truncation order P. We remark that, in order to achieve convergence, there are restrictions to the mesh discretization [28].

The amount of variance captured by the truncated KLE may not be the only criterion for the selection of truncation order, P. One may also consider stabilization of the energy distance between the generated samples and required value with P as shown in the numerical results below, or other appropriate criteria.

In order to generate sample paths of random fields via KL expansion, a technique for generation of the underlying standardized pairwise uncorrelated Gaussian random variables θ_i must be employed. As shown in [28], utilization of the stratification technique called Latin Hypercube Sampling (LHS) [31, 32] leads to faster convergence of the sample statistics to the target values with the number of samples compared to crude Monte Carlo sampling. Therefore, LHS was used to generate KLE realizations ($n_{\text{sim}} = 300$ samples were found sufficient to obtain converged mean and standard deviation). The LHS generator of pelvic BMD realizations is available on website BoneGen.

Validation Measures

BMC and *energy distance* [20] were considered as validation measure of a proposed BMD random field. The BMC measure is an integral value, defined as $\text{BMC} = \int_\Omega \rho \, \mathrm{d}\Omega$. This integral can be computed by finite element method. The BMC reflects the overall bone mass formed by mineral con-

tent and it is a sensitive measure of bone quality [33, 34, 35]. The energy distance d provides a way to measure the similarity between two probability distributions. For two one-dimensional distributions, u and v, the distance d is computed [20]:

$$d(u,v) = \sqrt{2\int_{-\infty}^{+\infty} \Big(U(x) - V(x)\Big)^2 \,\mathrm{d}x} \qquad (7)$$

where U and V are cumulative distribution functions.[1] In virtue of this study, the expression above describes a spatial distance density over the bone volume and hence we additionally introduce global distance measure as well: $D = \int_\Omega d\,\mathrm{d}\Omega$. This spatial integral over bone volume is again computed with the help of interpolation functions in the finite element method.

Results

The mean and standard deviation functions of BMD varied spatially significantly and differed for cortical and trabecular regions and for both females and males, i.e. BMD random fields were non-stationary in space.

Data analysis for *female* yielded the highest value of the sample mean value 1.246 (arcuate line, upper third), while the least was 0.106 (above the greater sciatic notch). The highest value of sample standard deviation (std) was 0.191 (top of the acetabular margin) while the lowest was 0.015 (deep to the auricular surface). The BMD normality is considered to be acceptable on significance level $p \geq 0.05$, which was fulfilled for 59% of bone volume. The skewness range is −1.893 (midpart of anterior margin of the greater sciatic notch) to 7.502 (posterior part of the iliac wing). The negative values corresponding to left-skewed distributions occupy 23% of volume, while the right-skewed distributions occupy 77% of volume.

The data analysis for *male* yields the lowest value of the mean value 0.119 (deep to the auricular surface), while the highest was 1.135 (uppermost part of arcuate line). The lowest value of std was 0.016 (in between the iliac wing and iliac tuberosity), while the highest was 0.218 (top of the acetabular margin). BMD distributions can be considered being normal for 54% of volume, while the rest contained non-normally distributed data. The skewness range is from −1.895 (inferior to ischial spine) to 6.177 (deep to the auricular surface). The left skewed distributions occupy 17% of volume, while the rest of the volume was occupied by right skewed distributions. The spatial descriptive statistics is shown in Figure 2.

Influence of Spectral Threshold on BMC

The BMC was computed from CT samples and the new ones generated by KLE with different number of eigenpairs. It was found that the most significant eigenvalue explains already 82%/86% of variance in the BMD, and taking five explains more than 97% variance for both female and male. There is no significant statistical difference between BMD computed from CT- and KLE-based realizations, even with KLE containing only the most significant eigenpair, see Figure 3.

Age dependence of BMC

The BMD slope for female varied in range from −5.163 (dorsally to the arcuate line) to 3.269 (above the greater sciatic notch) and from −5.470 (superior-posterior part of acetabular margin) to 3.625 (anterior third of iliac crest) [mg/cc/year] for female and male. The BMD is intermediately correlated with age ($R^2 \leq 0.51$) and ($R^2 \leq 0.49$) for female and male respectively. The age correlation was significant at 73% and 56% of volume on significance level $p \leq 0.05$ for female and male respectively, see Figure 4. In 71%/61% of volume, BMD decreased with age for both female and male. The difference in BMC age rate estimated from CT and KLE realizations is 5.57% and 4.71% for female and male respectively. The difference in standard error was 47% and 55% for female and male. The difference in R^2 is 21% and 50% for female and male; see Table 1.

Table 1: An age dependence of BMC estimated by linear regression on both CT and KLE samples. The KLE sample were generated with five eigenpairs included and LHS design.

	female		male	
source:	CT	KLE	CT	KLE
BMC rate [mg/year]	−0.2369	−0.2501	−0.1168	−0.1223
standard error	0.060	0.032	0.075	0.034
R^2	0.140	0.169	0.028	0.042

Energy Distance

The minimum/maximum distance $d_{\min}/d_{\max}$ stabilized after including more than 30 eigenpairs for female. The total distance D is decreasing with number KL pair included increasing and end up with a value 7425 for female.

The minimum/maximum distance $d_{\min}/d_{\max}$ is decreasing up to the 50$^{\text{th}}$ KL pair and consequently stabilized up to the last KL pair. The total distance decreasing with increasing the number of eigenpairs included up to a minimum value of 8303. The detailed evolution of energy distance is shown in Figure 5 together with snapshots at selected eigenpairs included. Including only first KL pair, there are energy distance peaks at dorsal portion of acetabular notch for female and below the anterior inferior iliac spine for male.

Discussion

Quantifying the uncertainties in bone mechanical properties originating from a representative population is of paramount importance to allow for clinically relevant conclusions and research-informed practice in bone treatment.

[1] For empirical distribution functions, the integral is replaced by a sum.

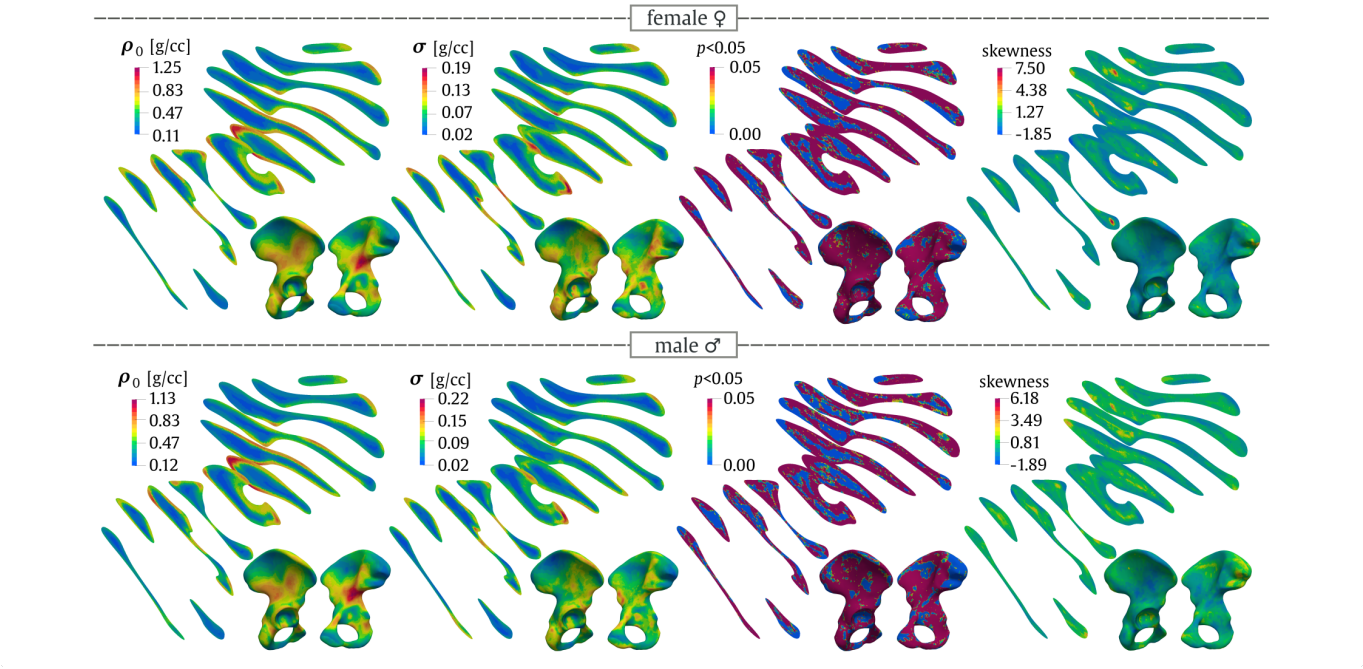

Figure 2: Spatial statistics of BMD composing of three statistical moments for both female and male

Due to complex bone shape and material with broad individual variations, any biomechanical experiments, both real and virtual (for example finite element simulations), should be equipped with a sufficient samples size. This requirement is often difficult to achieve, and lack of samples may reduce the potential for research conclusions to be applied to a broad population. We here introduce a random field model for BMD. With this model at hand, one can generate a number of BMD samples respecting the population variability and age dependence. The current model allows to replicate the BMD density in a domain, which is a sample mean population bone shape. In consequence, it is not necessary to capture shape variations. This step aiming to separate BMD and shape allows analyzing BMD variations at fixed metric as a random field, but it limits the model usability. Nevertheless, shape variations can be considered as a random field as well. The study of BMD and shape variations as random fields, potentially cross-correlated, will form the objective of subsequent studies. Although the random field model of BMD inferred from CT of patients with no bone disease seems a leap towards creating digital twins of bone [36, 37], a most beneficial approach would be to estimate random fields respecting pathological changes in bone structure and predicting the related risk of bone fractures [10, 8, 9].

Spatio-Temporal Dependence of BMD Random Field

Bone mechanical properties are well known to be age dependent ([38, 39, 40, 41]), and likely the studied random field will also be time temporally dependent. For this given study, only the deterministic part of an age trend was isolated. Generally, a temporal correlation structure can be modelled by KL expansion, but requires a sufficient sample size per analyzed time period. Knowing the temporal effect on BMD random field is extremely important and hence it is on a priority list for the next study.

Clinical CT Resolution

The multi-scale nature of bone could not be considered in details in the given study. The random field was estimated only at organ scale obtained from routine CT data that might not have a sufficient resolution to capture properly trabecular architecture or bone cortical shell. This issue complicates the estimation of local variations and anisotropy (fabric tensor [42, 43]) of trabecular network as well as the composite structure of the cortical shell. Although the gradient of the structure tensor might potentially be used to analyze bone anisotropy based on clinical data, this has not been tested in this study [44]. Clinical routine CT is known to distort the cortical density and thickness [45, 46], thereby exceeding a 100%-error in the sub millimeter structure of cortical bone. The effect of insufficient CT resolution might be seen at the central part of the iliac wing, where the thickness of the trabecular bone layers is minimized and prone to partial volume effects; this likely affects the random field. In some cases, even a fenestration may be present at this location [47]. It is not obvious how the statistical moments and correlation structure is affected and must be carefully analyzed with help of cortical thickness and density estimation algorithm introduced in [48], dedicated for clinical CT.

Spatial Variation of BMD

We assume that spatial fluctuation of BMD reflects bones' response to external loading, which causes bone to deform in a complex mode (bending + torsion + tension/compression).

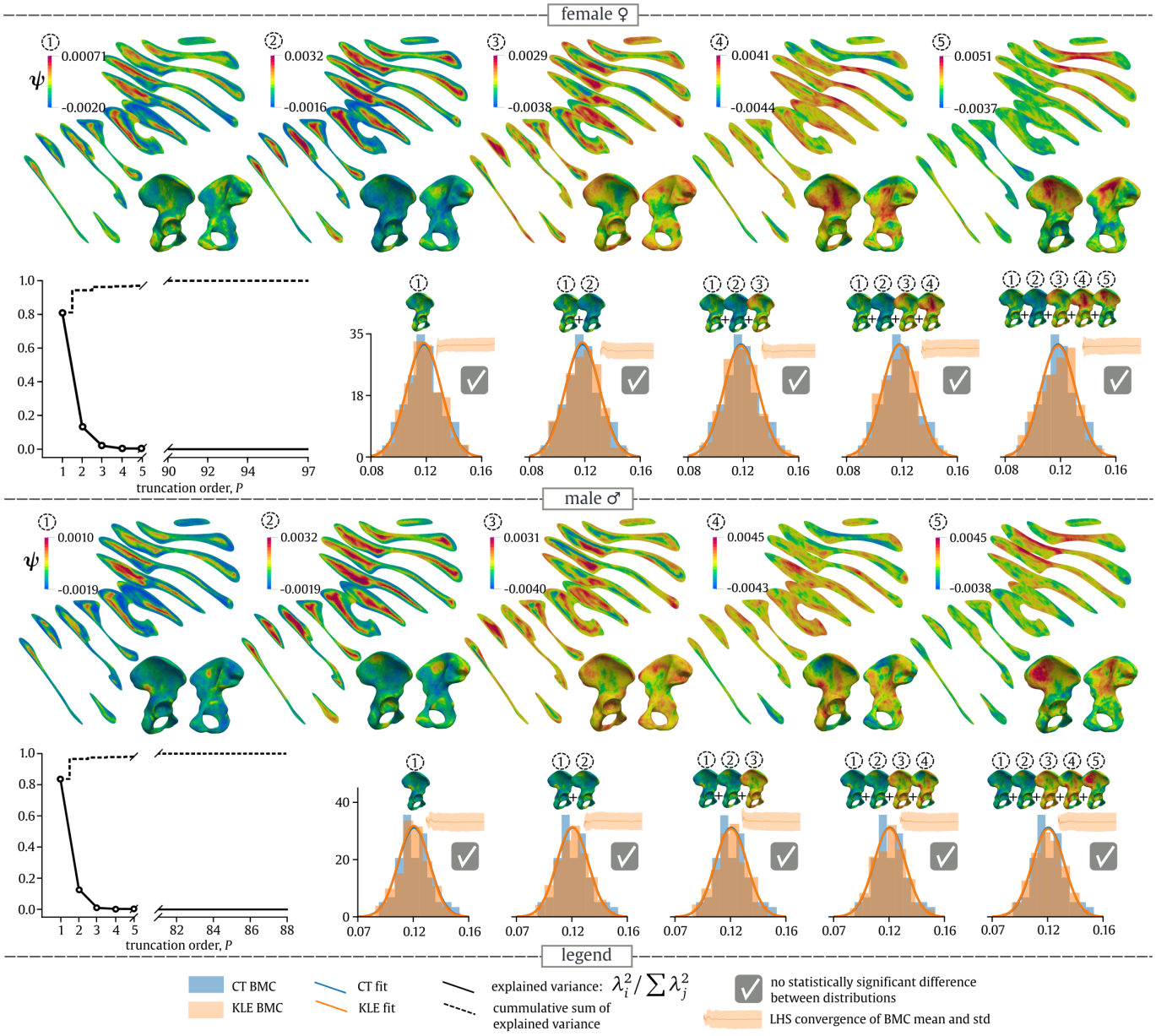

Figure 3: Analysis of explained variance by eigenpairs (λ, ψ) and its influence on BMC [g] computed by truncated KLE.

The load from trunk is directed through the sacroiliac (SI) joint to the acetabulum and the femoral head while standing, or through the ischial tuberosity while sitting. Simultaneously, more than thirty muscles and several ligaments are attached to the pelvis, loading the bone with their tension in various directions. Increased BMD in area of the greater sciatic notch, the upper part of arcuate line and body of ischium seems to correspond well to weight-bearing load. The relatively low standard deviation in this area could indicate that the weight-bearing load can be considered as a common base load in population. Even though the force generated by related muscles can be significant, just slight density elevations following the margins of large muscles' attachments (iliacus, gluteus medius) or isolated peaks for muscles with smaller insertion sites such as the rectus femoris were found. However, an interesting similarity between the high values of standard deviation and sites of possible apophyseal avulsions was observed. This could indicate an increased individual localized stress induced by inserted muscles or ligament insertions (anterior superior iliac spine – rectus femoris; anterior superior iliac spine – sartorius; ischial tuberosity – hamstrings; iliac crest – abdominal wall muscles; ischial spine – sacrospinous ligament and coccygeus muscle). The increased standard deviation in these sites could reflect variation in physical activity and other unknown effects. Other sites with increased standard deviation, i.e. superior acetabulum and anterior margin of auricular surface are typical of osteophytes.

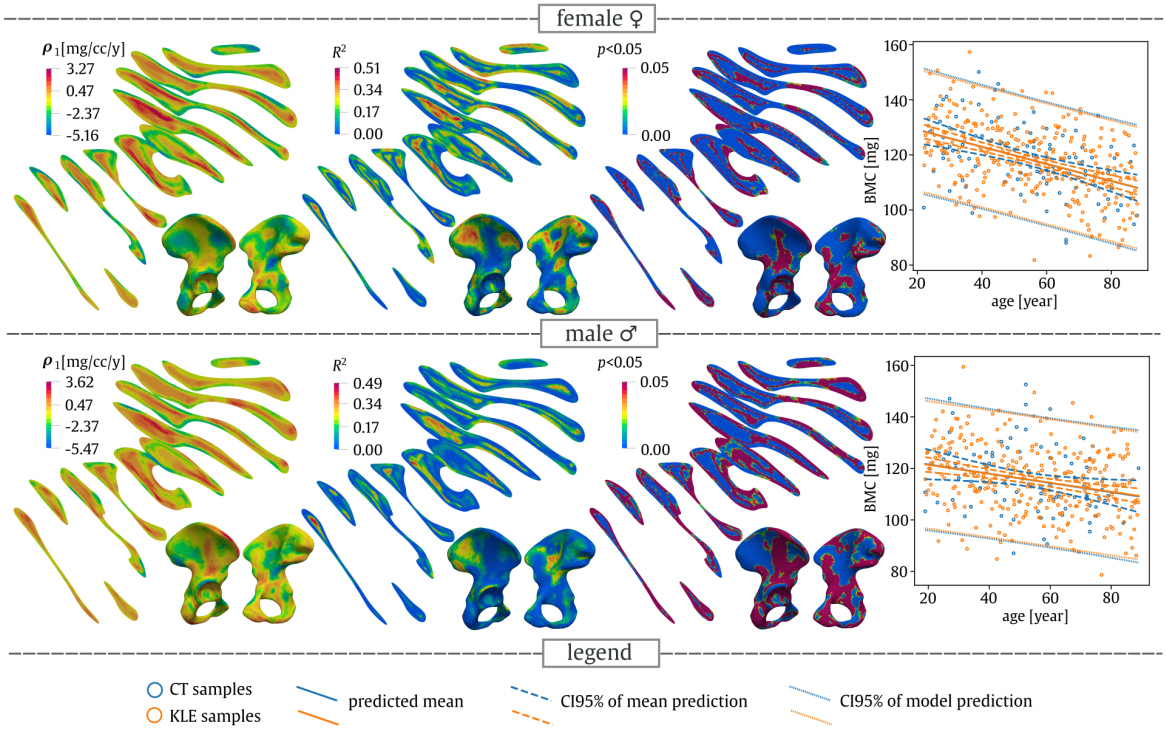

Figure 4: Spatio-temporal evolution of BMD and BMC.

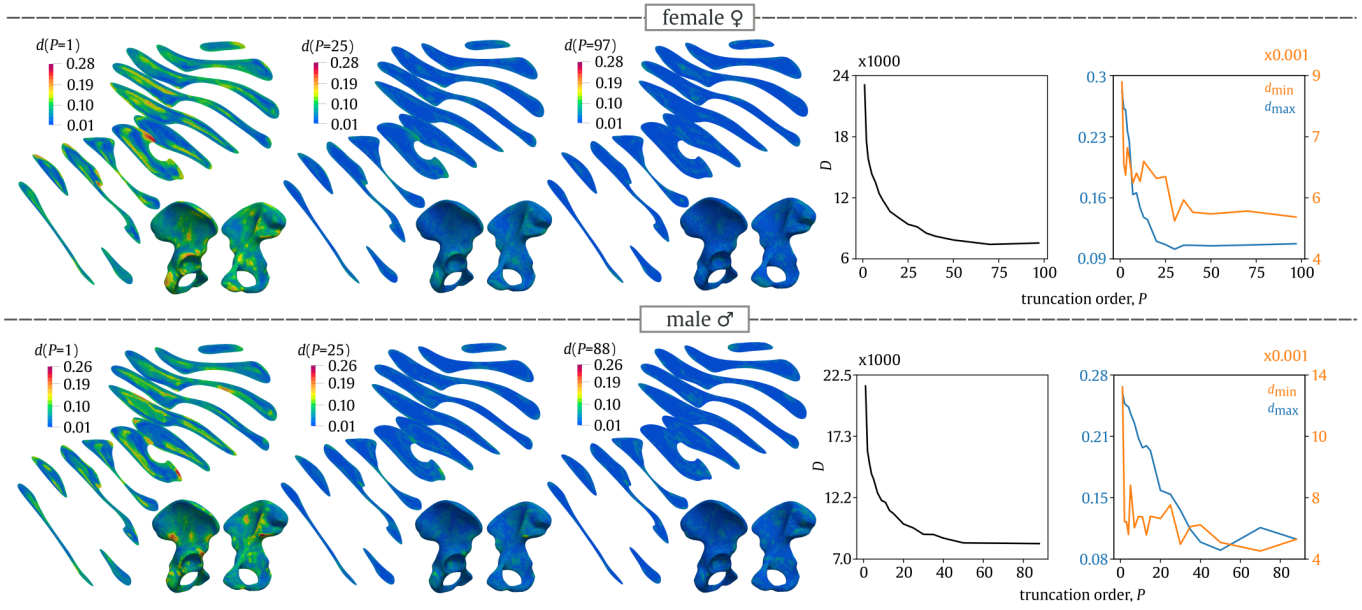

Figure 5: Spatial evaluation of the energy distance composed of spatial functions $d_{\min}$ and $d_{\max}$ and total distance D with respect to the number of eigenpairs included. The ratios $d_{\min}/d_{\max}$ are defined as minimum/maximum of distance over the domain. The minimum/maximum distance location changed with each eigenpair included, which leads to scatter in convergence plot.

Age Evolution of Bone Density

Most publications generally assume a gradual reduction in bone mineral density with increasing age [49, 50, 51]. It however remains unclear whether this is a uniform process for all skeletal sites or whether there might be some region dependence [52, 53, 54]. Moreover, due to the variable surface-volume ratio and related bone turnover the local differences between cortical and cancellous bone should be expected [55, 56, 57]. The age changes in cortical BMD can be described by cortical thinning, higher porosity, pores diameter and osteon density [58, 59, 57, 60, 61]. Cancellous bone is affected by trabecular loss. In male it is mostly in a form of trabecular thinning, in female of trabecular disconnection [62, 63, 64, 65]. There is, however, little known

about the spatial and age distribution of BMD in human innominate bone as majority of studies focus on long bone, vertebral or hip examinations. Our results showed general age dependent cortical BMD decline and, surprisingly, local mild trabecular BMD elevation. The reason is unclear and could be connected to higher trabecular mineralization patterns, which correlates with age, as documented in [66]. We found that female BMD is more sensitive to age. The BMD decreases with age in more than 68%/58% volume of bone for female/male. The BMC decreases faster for female (51% faster than for male).

Correlation Structure of BMD

In the given study, a non-parametric approach to generate new realizations of BMD has been demonstrated. This approach was purely based on input CT data, and the next step is to determine parametric correlation kernels, which could represent the correlation structure in time and space. A simple stationary random field model for whole bone exists unlikely being for several reasons: Bone forms a geometrically highly complex structure, and the Euclidean distance will unlikely properly capture bone topology [67]. Moreover, due to the adaptation processes at bone undergoes, there might be a spatially-dependent anisotropy in correlation structure as well as distance metric will be spatially dependent. Finally, multiple latent variables coexist, for example adaptation process, geometrical influence and other metabolic variables [68]. Together, those variables most likely cause long correlation distances, as seen in Figure 6. The identification and separation of these latent variables is difficult due to the limited information available from CT and from patient medical records. This will be the topic of future study. Another question raised is from how well the empirical correlation $\mathbf{C}$ and its eigenpairs represents the true population correlation due to course of dimensionality and noise (potentially spurious correlation) [69].

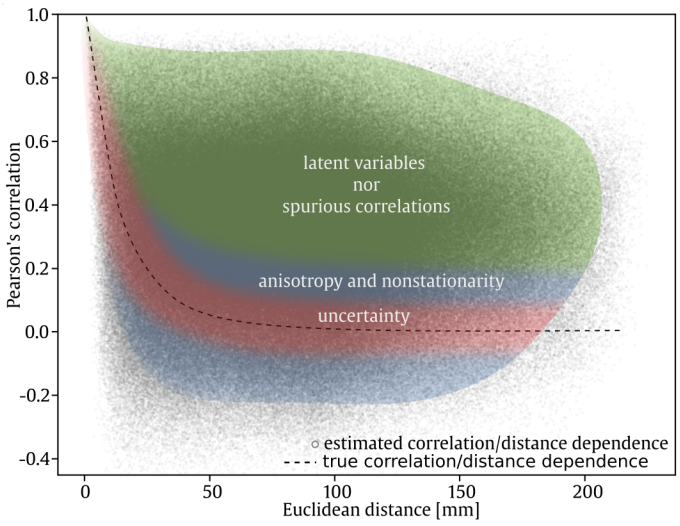

Figure 6: A correlation dependence on distance for BMD random field for female estimated from CT samples.

Assumption of Gaussian KL Coefficients

The distribution of BMD is site dependent. There are locations which follow approximately normal distribution, while other locations are slightly left-skewed and significantly right-skewed in distribution as well. The proposed KLE-based model used uncorrelated Gaussian coefficients, which introduces a certain inaccuracy, that is seen in the energy distance metric. The energy metric reveals that the distributions estimated from CT samples and those from KLE model are different at some locations. It has been shown that taking five dominant KL coefficients is sufficient for an accurate reproduction of variance in BMD/BMC. However, the analysis of the energy distance shows that far more KL coefficients (>30) are needed to reproduce the distribution function of the BMD random field. Energy distance is stricter than BMD/BMC because it directly describes the similarity of BMD distributions. Hence, the energy distance could be a good indicator of that the local properties such as fracture risk probability estimation might not be accurate enough and mean/std estimation might be biased. To improve our model, the identification of (generally non-Gaussian) distributions of KL coefficients should be incorporated into random field model based on KLE, for example by iterative algorithm introduced in [70].

Random Field Model Implementation

The covariance matrix of BMD is dense and large, hence it disallows a common storage representation and solving of Fredholm integral. Although we partially avoided these difficulties by directly manipulating with data on discrete level, a more robust approach must be applied, for instance the recent approximation of KL by isogeometric method [71].

Comparison with Statistical Shape & Appearance Models (SSM/SSA)

Our method shares the steps of geometry aligning and spectral decomposition of empirical covariance matrix with SSM/SSA [72, 73, 74], but the meaning and computing of these steps is different. The bone shape aligning is computed on ROI of whole pelvic bone allowing to align the interior as well (cortical thickness and trabecular structure, although highly blurred caused by clinical CT resolution). Our approach uses the covariance eigenpairs as bases for generating new BMD realizations. And most importantly, our approach is rather focused on exploring/explaining the spatio-temporal correlation structure, which reflects somehow (mechano-)biological mechanisms of growth and adaptation [75] in authors' opinion.

Conclusion

The understanding of uncertainties in bone density arising from population is of paramount importance to biomechanics, in understanding of bone mechanobiology and it should be properly incorporated into computational models. We introduced a random field model describing the fluctuation in

bone density via the KLE. The following sub-conclusions can be made:

- the BMD has a complex correlation structure which cannot be modelled by an isotropic, spatially/temporally stationary Gaussian random field,
- Gaussian KL coefficients allows to simulate BMC accurately,
- the modelled BMD random field allows to incorporate age dependence of BMD.

Conflict of interest statement

The authors declare no conflict of interest.

Acknowledgements

Authors acknowledge financial support from project no. LTAUSA19058 provided by the Ministry of Education, Youth and Sports of the Czech Republic. Additionally, the work has been supported by the Czech Science Foundation under project no. 20-01781S.

References

[1] J.-Y. Rho, L. Kuhn-Spearing, P. Zioupos, Mechanical properties and the hierarchical structure of bone, Medical Engineering & Physics 20 (2) (1998) 92–102. doi:10.1016/S1350-4533(98)00007-1.

[2] N. Reznikov, R. Shahar, S. Weiner, Bone hierarchical structure in three dimensions, Acta Biomaterialia 10 (9) (2014) 3815–3826, biomineralization. doi:10.1016/j.actbio.2014.05.024.

[3] B. Busse, M. Hahn, M. Soltau, J. Zustin, K. Püschel, G. N. Duda, M. Amling, Increased calcium content and inhomogeneity of mineralization render bone toughness in osteoporosis: mineralization, morphology and biomechanics of human single trabeculae, Bone 45 (6) (2009) 1034–1043. doi:10.1016/j.bone.2009.08.002.

[4] K. Tai, M. Dao, S. Suresh, A. Palazoglu, C. Ortiz, Nanoscale heterogeneity promotes energy dissipation in bone, Nature Materials 6 (6) (2007) 454–462. doi:10.1038/nmat1911.

[5] B. Davies, A. King, P. Newman, A. Minett, C. R. Dunstan, H. Zreiqat, Hypothesis: Bones toughness arises from the suppression of elastic waves, Scientific reports 4 (2014) 7538. doi:10.1038/srep07538.

[6] A. M. Torres, J. B. Matheny, T. M. Keaveny, D. Taylor, C. M. Rimnac, C. J. Hernandez, Material heterogeneity in cancellous bone promotes deformation recovery after mechanical failure, Proceedings of the National Academy of Sciences 113 (11) (2016) 2892–2897. doi:10.1073/pnas.1520539113.

[7] D. Ruffoni, P. Fratzl, P. Roschger, K. Klaushofer, R. Weinkamer, The bone mineralization density distribution as a fingerprint of the mineralization process, Bone 40 (5) (2007) 1308–1319. doi:10.1016/j.bone.2007.01.012.

[8] C. Falcinelli, E. Schileo, L. Balistreri, F. Baruffaldi, B. Bordini, M. Viceconti, U. Albisinni, F. Ceccarelli, L. Milandri, A. Toni, F. Taddei, Multiple loading conditions analysis can improve the association between finite element bone strength estimates and proximal femur fractures: A preliminary study in elderly women, Bone 67 (2014) 71–80. doi:10.1016/j.bone.2014.06.038.

[9] E. S. Orwoll, L. M. Marshall, C. M. Nielson, S. R. Cummings, J. Lapidus, J. A. Cauley, K. Ensrud, N. Lane, P. R. Hoffmann, D. L. Kopperdahl, et al., Finite element analysis of the proximal femur and hip fracture risk in older men, Journal of bone and mineral research 24 (3) (2009) 475–483. doi:10.1359/jbmr.081201.

[10] G. Dahan, N. Trabelsi, O. Safran, Z. Yosibash, Finite element analyses for predicting anatomical neck fractures in the proximal humerus, Clinical Biomechanics 68 (2019) 114–121. doi:10.1016/j.clinbiomech.2019.05.028.

[11] X. N. Dong, R. Pinninti, T. Lowe, P. Cussen, J. E. Ballard, D. Di Paolo, M. Shirvaikar, Random field assessment of inhomogeneous bone mineral density from DXA scans can enhance the differentiation between postmenopausal women with and without hip fractures, Journal of Biomechanics 48 (6) (2015) 1043–1051. doi:10.1016/j.jbiomech.2015.01.030.

[12] X. N. Dong, M. Shirvaikar, X. Wang, Biomechanical properties and microarchitecture parameters of trabecular bone are correlated with stochastic measures of 2D projection images, Bone 56 (2) (2013) 327–336. doi:10.1016/j.bone.2013.05.023.

[13] X. N. Dong, R. Pinninti, A. Tvinnereim, T. Lowe, D. Di Paolo, M. Shirvaikar, Stochastic predictors from the DXA scans of human lumbar vertebrae are correlated with the microarchitecture parameters of trabecular bone, Journal of Biomechanics 48 (12) (2015) 2968–2975. doi:10.1016/j.jbiomech.2015.07.041.

[14] X. N. Dong, Y. Lu, M. Krause, G. Huber, Y. Chevalier, H. Leng, G. Maquer, Variogram-based evaluations of DXA correlate with vertebral strength, but do not enhance the prediction compared to aBMD alone, Journal of Biomechanics 77 (2018) 223–227. doi:10.1016/j.jbiomech.2018.07.009.

[15] G. Maquer, Y. Lu, E. Dall'Ara, Y. Chevalier, M. Krause, L. Yang, R. Eastell, K. Lippuner, P. K. Zysset, The initial slope of the variogram, foundation of the trabecular bone score, is not or is poorly associated with vertebral strength, Journal of bone and mineral research 31 (2) (2016) 341–346. doi:10.1002/jbmr.2610.

[16] X. N. Dong, Q. Luo, D. M. Sparkman, H. R. Millwater, X. Wang, Random field assessment of nanoscopic inhomogeneity of bone, Bone 47 (6) (2010) 1080–1084. doi:10.1016/j.bone.2010.08.021.

[17] C. Desceliers, C. Soize, S. Naili, G. Haïat, Probabilistic model of the human cortical bone with mechanical alterations in ultrasonic range, Mechanical Systems and Signal Processing 32 (2012) 170–177. doi:10.1016/j.ymssp.2012.03.008.

[18] M. Kirby, A. H. Morshed, J. Gomez, P. Xiao, Y. Hu, X. E. Guo, X. Wang, Three-dimensional rendering of trabecular bone microarchitecture using a probabilistic approach, Biomechanics and Modeling in Mechanobiology (2020) 1–19doi:10.1007/s10237-020-01286-8.

[19] J. Luque, I. Papaioannou, D. Straub, M. Ruess, D. Schillinger, Probabilistic model of bone structure based on CT scan data and validation of simulation results using the finite cell method, in: ICOSSAR 2012, University of N.Y.C., New York City, 2013, pp. 2017–2024.

[20] G. J. Székely, M. L. Rizzo, Energy statistics: A class of statistics based on distances, Journal of Statistical Planning and Inference 143 (8) (2013) 1249–1272. doi:10.1016/j.jspi.2013.03.018.

[21] Y. Pauchard, T. Fitze, D. Browarnik, A. Eskandari, I. Pauchard, W. Enns-Bray, H. Pálsson, S. Sigurdsson, S. J. Ferguson, T. B. Harris, et al., Interactive graph-cut segmentation for fast creation of finite element models from clinical CT data for hip fracture prediction, Computer methods in biomechanics and biomedical engineering 19 (16) (2016) 1693–1703. doi:10.1080/10255842.2016.1181173.

[22] A. S. Michalski, B. A. Besler, G. J. Michalak, S. K. Boyd, CT-based internal density calibration for opportunistic skeletal assessment using abdominal CT scans, Medical Engineering & Physics 78 (2020) 55–63. doi:10.1016/j.medengphy.2020.01.009.

[23] B. B. Avants, N. J. Tustison, G. Song, P. A. Cook, A. Klein, J. C. Gee, A reproducible evaluation of ANTs similarity metric performance in brain image registration, Neuroimage 54 (3) (2011) 2033–2044, pMID: 20851191 PMCID: PMC3065962. doi:10.1016/j.neuroimage.2010.09.025.

[24] M. Kuchař, P. Henyš, P. Rejtar, P. Hájek, Shape morphing technique can accurately predict pelvic bone landmarks, International Journal of Legal Medicine (2021). doi:10.1007/s00414-021-02501-6.

[25] B. B. Avants, P. Yushkevich, J. Pluta, D. Minkoff, M. Korczykowski, J. Detre, J. C. Gee, The optimal template effect in hippocampus studies of diseased populations, Neuroimage 49 (3) (2010) 2457–2466. doi:10.1016/j.neuroimage.2009.09.062.

[26] B. L. Will Schroeder, Ken Martin, The visualization toolkit: an object-

oriented approach to 3D graphics, Kitware, 2003.

[27] Y. Hu, T. Schneider, B. Wang, D. Zorin, D. Panozzo, Fast tetrahedral meshing in the wild, arXiv (2019) arXiv–1908doi:10.1145/3386569.3392385.

[28] M. Vořechovský, Simulation of simply cross correlated random fields by series expansion methods, Structural safety 30 (4) (2008) 337–363. doi:10.1016/j.strusafe.2007.05.002.

[29] H. Harbrecht, M. Peters, M. Siebenmorgen, Efficient approximation of random fields for numerical applications, Numerical Linear Algebra with Applications 22 (4) (2015) 596–617. doi:10.1002/nla.1976.

[30] R. G. Ghanem, P. D. Spanos, Stochastic finite elements: a spectral approach, Courier Corporation, 2003. doi:10.1007/978-1-4612-3094-6.

[31] W. Conover, On a better method for selecting input variables, unpublished Los Alamos National Laboratories manuscript, reproduced as Appendix A of "Latin Hypercube Sampling and the Propagation of Uncertainty in Analyses of Complex Systems" by J.C. Helton and F.J. Davis, Sandia National Laboratories report SAND2001-0417, printed November 2002. (1975).
URL https://prod-ng.sandia.gov/techlib-noauth/access-control.cgi/2001/010417.pdf

[32] M. D. McKay, W. J. Conover, R. J. Beckman, A comparison of three methods for selecting values of input variables in the analysis of output from a computer code, Technometrics 21 (1979) 239–245. doi:10.1080/00401706.1979.10489755.

[33] R. Hou, S. A. Cole, M. Graff, K. Haack, S. Laston, A. G. Comuzzie, N. R. Mehta, K. Ryan, D. L. Cousminer, B. S. Zemel, S. F. Grant, B. D. Mitchell, R. J. Shypailo, M. L. Gourlay, K. E. North, N. F. Butte, V. S. Voruganti, Genetic variants affecting bone mineral density and bone mineral content at multiple skeletal sites in Hispanic children, Bone 132 (2020) 115175. doi:10.1016/j.bone.2019.115175.

[34] M. Bellver, L. Del Rio, E. Jovell, F. Drobnic, A. Trilla, Bone mineral density and bone mineral content among female elite athletes, Bone 127 (2019) 393–400. doi:10.1016/j.bone.2019.06.030.

[35] H. Kaur, P. Joshee, S. Franquemont, A. Baumgartner, J. Thurston, L. Pyle, K. J. Nadeau, V. N. Shah, Bone mineral content and bone density is lower in adolescents with type 1 diabetes: A brief report from the RESISTANT and EMERALD studies, Journal of Diabetes and its Complications 32 (10) (2018) 931–933. doi:10.1016/j.jdiacomp.2018.06.004.

[36] M. A. Juárez, M. Pennisi, G. Russo, D. Kiagias, C. Curreli, M. Viceconti, F. Pappalardo, Generation of digital patients for the simulation of tuberculosis with UISS-TB, BMC Bioinformatics 21 (S17) (2020) 1–8. doi:10.1186/s12859-020-03776-z.

[37] M. Viceconti, F. Pappalardo, B. Rodriguez, M. Horner, J. Bischoff, F. M. Tshinanu, *In silico* trials: Verification, validation and uncertainty quantification of predictive models used in the regulatory evaluation of biomedical products, Methods (2020). doi:10.1016/j.ymeth.2020.01.011.

[38] T. M. Keaveny, D. L. Kopperdahl, L. J. Melton III, P. F. Hoffmann, S. Amin, B. L. Riggs, S. Khosla, Age-dependence of femoral strength in white women and men, Journal of bone and mineral research 25 (5) (2010) 994–1001. doi:10.1359/jbmr.091033.

[39] F. Yu, Y. Xu, Y. Hou, Y. Lin, R. Jiajue, Y. Jiang, O. Wang, M. Li, X. Xing, L. Zhang, L. Qin, E. Hsieh, W. Xia, Age-, site-, and sex-specific normative centile curves for HR-pQCT -derived microarchitectural and bone strength parameters in a chinese mainland population, Journal of Bone and Mineral Research 35 (11) (2020) 2159–2170. doi:10.1002/jbmr.4116.

[40] J. Sanchez-Siles, I. Tamimi-Mariño, A. Cortes, J. Ackerman, D. González-Quevedo, E. Guerado, A. García, F. Yaghoubi, M. Abdallah, H. Eimar, et al., Age related changes in the bone microstructure in patients with femoral neck fractures, Injury (2020). doi:10.1016/j.injury.2020.02.014.

[41] D. M. Patton, E. M. Bigelow, S. H. Schlecht, D. H. Kohn, T. L. Bredbenner, K. J. Jepsen, The relationship between whole bone stiffness and strength is age and sex dependent, Journal of Biomechanics 83 (2019) 125–133. doi:10.1016/j.jbiomech.2018.11.030.

[42] T. Gross, D. H. Pahr, P. K. Zysset, Morphology-elasticity relationships using decreasing fabric information of human trabecular bone from three major anatomical locations, Biomechanics and modeling in mechanobiology 12 (4) (2013) 793–800. doi:10.1007/s10237-012-0443-2.

[43] P. Varga, P. Zysset, Assessment of volume fraction and fabric in the distal radius using HR-pQCT, Bone 45 (5) (2009) 909–917. doi:10.1016/j.bone.2009.07.001.

[44] D. Larsson, B. Luisier, M. E. Kersh, E. Dall'Ara, P. K. Zysset, M. G. Pandy, D. H. Pahr, Assessment of transverse isotropy in clinical-level CT images of trabecular bone using the gradient structure tensor, Annals of biomedical engineering 42 (5) (2014) 950–959. doi:10.1007/s10439-014-0983-y.

[45] G. Dougherty, D. Newman, Measurement of thickness and density of thin structures by computed tomography: a simulation study, Medical Physics 26 (7) (1999) 1341–1348. doi:10.1118/1.598629.

[46] S. Prevrhal, J. C. Fox, J. A. Shepherd, H. K. Genant, Accuracy of CT-based thickness measurement of thin structures: Modeling of limited spatial resolution in all three dimensions, Medical Physics 30 (1) (2003) 1–8. doi:10.1118/1.1521940.

[47] J. Hernigou, A. Alves, Y. Homma, I. Guissou, P. Hernigou, Anatomy of the ilium for bone marrow aspiration: map of sectors and implication for safe trocar placement, International Orthopaedics 38 (12) (2014) 2585–2590. doi:10.1007/s00264-014-2353-7.

[48] G. Treece, A. Gee, Independent measurement of femoral cortical thickness and cortical bone density using clinical CT, Medical Image Analysis 20 (1) (2015) 249–264. doi:10.1016/j.media.2014.11.012.

[49] O. Demontiero, C. Vidal, G. Duque, Aging and bone loss: new insights for the clinician, Therapeutic advances in musculoskeletal disease 4 (2) (2012) 61–76. doi:10.1177/1759720X11430858.

[50] S. Khosla, B. L. Riggs, Pathophysiology of age-related bone loss and osteoporosis, Endocrinology and Metabolism Clinics 34 (4) (2005) 1015–1030. doi:10.1016/j.ecl.2005.07.009.

[51] B. L. Riggs, L. J. Melton III, R. A. Robb, J. J. Camp, E. J. Atkinson, J. M. Peterson, P. A. Rouleau, C. H. McCollough, M. L. Bouxsein, S. Khosla, Population-based study of age and sex differences in bone volumetric density, size, geometry, and structure at different skeletal sites, Journal of Bone and Mineral Research 19 (12) (2004) 1945–1954. doi:10.1359/JBMR.040916.

[52] X.-H. Ma, W. Zhang, Y. Wang, P. Xue, Y.-K. Li, Comparison of the spine and hip BDM assessments derived from quantitative computed tomography, International Journal of Endocrinology 2015 (2015). doi:10.1155/2015/675340.

[53] E. G. Vajda, R. D. Bloebaum, Age-related hypermineralization in the female proximal human femur, The Anatomical Record 255 (2) (1999) 202–211. doi:10.1002/(sici)1097-0185(19990601)255:2<202::aid-ar10>3.0.co;2-0.

[54] A. Paschall, A. H. Ross, Biological sex variation in bone mineral density in the cranium and femur, Science & Justice 58 (4) (2018) 287–291. doi:10.1016/j.scijus.2018.01.002.

[55] S. M. Ott, Cortical or trabecular bone: what's the difference?, American journal of nephrology 47 (6) (2018) 373–376. doi:10.1159/000489672.

[56] X. Wang, Cortical bone mechanics and composition: effects of age and gender, in: Skeletal Aging and Osteoporosis, Springer, 2012, pp. 53–85. doi:10.1007/8415_2011_108.

[57] E. Seeman, Structural basis of growth-related gain and age-related loss of bone strength, Rheumatology 47 (Supplement 4) (2008) iv2–iv8, proceedings of a satellite symposium held on the occasion of the EULAR Congress, Paris, France, June 13, 2008. doi:10.1093/rheumatology/ken177.

[58] E. F. Kranioti, A. Bonicelli, J. G. García-Donas, Bone-mineral density: clinical significance, methods of quantification and forensic applications, Research and Reports in Forensic Medical Science 9 (2019) 9–21. doi:10.2147/RRFMS.S164933.

[59] A. Ural, D. Vashishth, Hierarchical perspective of bone toughness–from molecules to fracture, International Materials Reviews 59 (5) (2014) 245–263. doi:10.1179/1743280414Y.0000000031.

[60] K. J. Jepsen, N. Andarawis-Puri, The amount of periosteal apposition required to maintain bone strength during aging depends on adult bone morphology and tissue-modulus degradation rate, Journal of Bone and Mineral Research 27 (9) (2012) 1916–1926. doi:

10.1002/jbmr.1643.

[61] K. M. Nicks, S. Amin, E. J. Atkinson, B. L. Riggs, L. J. Melton III, S. Khosla, Relationship of age to bone microstructure independent of areal bone mineral density, Journal of Bone and Mineral Research 27 (3) (2012) 637–644. doi:10.1002/jbmr.1468.

[62] J. E. Aaron, N. B. Makins, K. Sagreiya, The microanatomy of trabecular bone loss in normal aging men and women, Clinical Orthopaedics and Related Research 215 (1987) 260–271, pMID: 3802645. doi:10.1097/00003086-198702000-00038.

[63] M. Ding, A. Odgaard, F. Linde, I. Hvid, Age-related variations in the microstructure of human tibial cancellous bone, Journal of Orthopaedic Research 20 (3) (2002) 615–621. doi:10.1016/S0736-0266(01)00132-2.

[64] K. J. Jepsen, Functional interactions among morphologic and tissue quality traits define bone quality, Clinical Orthopaedics and Related Research® 469 (8) (2011) 2150–2159. doi:10.1007/s11999-010-1706-9.

[65] H. Chen, X. Zhou, H. Fujita, M. Onozuka, K.-Y. Kubo, Age-related changes in trabecular and cortical bone microstructure, International journal of endocrinology 2013 (2013). doi:10.1155/2013/213234.

[66] T. Koehne, E. Vettorazzi, N. Küsters, R. Lüneburg, B. Kahl-Nieke, K. Püschel, M. Amling, B. Busse, Trends in trabecular architecture and bone mineral density distribution in 152 individuals aged 30–90 years, Bone 66 (2014) 31–38. doi:10.1016/j.bone.2014.05.010.

[67] S. Pezzuto, A. Quaglino, M. Potse, On sampling spatially-correlated random fields for complex geometries, in: International Conference on Functional Imaging and Modeling of the Heart, Springer, 2019, pp. 103–111. doi:10.1007/978-3-030-21949-9_12.

[68] V. S. Cheong, B. C. Roberts, V. Kadirkamanathan, E. Dall'Ara, Bone remodelling in the mouse tibia is spatio-temporally modulated by oestrogen deficiency and external mechanical loading: A combined *in vivo*/*in silico* study, Acta Biomaterialia 116 (2020) 302–317. doi:10.1016/j.actbio.2020.09.011.

[69] J. Bun, J.-P. Bouchaud, M. Potters, Cleaning large correlation matrices: Tools from random matrix theory, Physics Reports 666 (2017) 1–109, cleaning large correlation matrices: tools from random matrix theory. doi:10.1016/j.physrep.2016.10.005.

[70] Z. Zheng, H. Dai, Y. Wang, W. Wang, A sample-based iterative scheme for simulating non-stationary non-Gaussian stochastic processes, Mechanical Systems and Signal Processing 151 (2021) 107420. doi:10.1016/j.ymssp.2020.107420.

[71] M. Ł. Mika, T. J. R. Hughes, D. Schillinger, P. Wriggers, R. R. Hiemstra, A matrix-free isogeometric Galerkin method for Karhunen-Loève approximation of random fields using tensor product splines, tensor contraction and interpolation based quadrature, arXiv preprint arXiv:2011.13861 (2020).
URL https://arxiv.org/abs/2011.13861v1

[72] N. Sarkalkan, H. Weinans, A. A. Zadpoor, Statistical shape and appearance models of bones, Bone 60 (2014) 129–140. doi:10.1016/j.bone.2013.12.006.

[73] V. Chandran, G. Maquer, T. Gerig, P. Zysset, M. Reyes, Supervised learning for bone shape and cortical thickness estimation from CT images for finite element analysis, Medical Image Analysis 52 (2019) 42–55. doi:10.1016/j.media.2018.11.001.

[74] S. P. Väänänen, L. Grassi, G. Flivik, J. S. Jurvelin, H. Isaksson, Generation of 3D shape, density, cortical thickness and finite element mesh of proximal femur from a DXA image, Medical Image Analysis 24 (1) (2015) 125–134. doi:10.1016/j.media.2015.06.001.

[75] T. J. Paul, P. Kollmannsberger, Biological network growth in complex environments: A computational framework, PLOS Computational Biology 16 (11) (2020) e1008003. doi:10.1371/journal.pcbi.1008003.